

Magnetic field-induced quasiparticle excitation in Nb_3Sn : Evidence for anisotropic s -wave pairing

R. Kadono*,^{1,2} K. H. Satoh,² A. Koda,^{1,2} T. Nagata,³ H. Kawano-Furukawa,³ J. Suzuki,⁴ M. Matsuda,⁴ K. Ohishi,⁴ W. Higemoto,⁴ S. Kuroiwa,⁵ H. Takagiwa,⁵ and J. Akimitsu⁵

¹Institute of Materials Structure Science, High Energy Accelerator Research Organization (KEK), Tsukuba, Ibaraki 305-0801, Japan

²School of High Energy Accelerator Science, The Graduate University for Advanced Studies, Tsukuba, Ibaraki 305-0801, Japan

³Department of Physics, Ochanomizu University, Bunkyo-ku, Tokyo, 112-8610, Japan

⁴Advanced Science Research Center, Japan Atomic Energy Agency, Tokai, Ibaraki 319-1195, Japan

⁵Department of Physics, Aoyama-Gakuin University, Sagamihara, Kanagawa, 229-8558 Japan

(Dated: February 8, 2020)

The response of vortex state to the magnetic field in Nb_3Sn is probed using muon spin rotation and small-angle neutron scattering. A transformation of vortex structure between hexagonal and squared lattice is observed over a relatively low field range of 2–3 Tesla. The gradual increase of the magnetic penetration depth with increasing field provides microscopic evidence for anisotropic (or multi-gapped) s -wave pairing suggested by the Raman scattering experiment. This result renders need for careful examination on the difference of electronic properties between Nb_3Sn and V_3Si .

PACS numbers: 74.25.Jb, 74.25.Nf, 76.75.+i, 61.12.Ex

While the technologies for utilizing high- T_c cuprates are making steady progress in recent years, triniobium stannide (Nb_3Sn) is still one of the most important materials for the practical application of superconductivity after fifty years since its discovery.¹ Because of its convenient characters such as modestly high transition temperature ($T_c \simeq 18.3$ K) and remarkably high upper critical field ($\mu_0 H_{c2} \simeq 24.5$ T), Nb_3Sn is used at the heart of superconducting devices, most notably as superconducting wires in high-field magnets. Nb_3Sn belongs to a class of A_3B binary intermetallic compounds with the A15 or β -tungsten structure, where those based on Nb give rise to a subclass that includes Nb_3Ge ², which used to dominate the highest T_c ($\simeq 23$ K) for more than thirty years, and therefore it was once a subject of intensive study until '70s.^{3,4,5} Surprisingly, however, it seems that the microscopic details on the superconducting characters of Nb_3Sn are not fully understood to date. For example, the revelation of a structural transformation from cubic to tetragonal with decreasing temperature not far above T_c (martensitic phase transition, which occurs at $T_M = 43$ K in Nb_3Sn ⁶) led to the argument that the coupling to the instability of lattice vibrations (soft phonons) associated with the martensitic transition might contribute to the increase of T_c . Experimental verification of the elastic softening^{7,8} prompted various models for microscopic mechanism of the martensitic transition, many of which emphasize the importance of the quasi-one-dimensional character of Nb atoms in the A15 structure that might also lead to the anomaly in the electronic density of states, the Kohn anomaly due to electron-phonon interaction, or to the Peierls instability.^{3,4,5} Unfortunately, while these models were partially successful to explain the elastic properties of Nb_3Sn , none of them has appeared as unambiguous explanation for the high T_c .

Here, we report on the first systematic study of vortex (flux line) state in Nb_3Sn using muon spin rotation

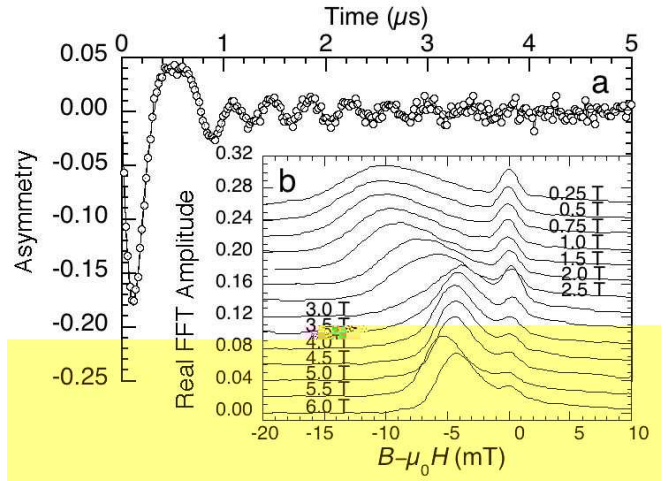


FIG. 1: a) Example of μ SR time spectrum ($\mu_0 H = 2$ T) displayed in the rotating reference frame of 201 MHz (where solid curve represents fitting result using a model described in the text, yielding a reduced chi-square of 1.21), and b) real amplitude of the fast Fourier transform (FFT, raw data) of the time spectra under several magnetic fields in the mixed state of Nb_3Sn ($\propto n(B)$), where each spectrum is shifted vertically for clarity. The background signal from muons stopping in a lucite scintillator (used both as a sample holder and a muon veto counter) gives rise to the peak at $B - \mu_0 H = 0$, where the amplitude is determined by the efficiency of the muon veto counter ($\simeq 95\%$, which leads to a relative background yield of $\sim 5\%$).

(μ SR) and small-angle neutron scattering (SANS). The combined use of μ SR and SANS on the identical specimen is proven to be ideal for the study of the mixed state, as they provide complementary information on the magnetic field distribution associated with flux line lattice (FLL): μ SR is sensitive to local field distribution

while SANS is sensitive to the long range structure of FLL. Moreover, it eliminates much of the problems associated with the difference in the preparation of specimen. In this brief communication, we show that one of the keys to understand the superconductivity of Nb_3Sn is the anisotropy in the electronic state, which is demonstrated by the transformation of FLL structure from hexagonal to squared with increasing flux density. Similar observation in V_3Si strongly suggests that this is a common feature of the superconductors with A15 structure,^{9,10} where the anisotropy of the Fermi surface is reflected through the nonlocal effect.^{11,12} Meanwhile, the field-induced enhancement of the magnetic penetration depth at lower fields, which is absent in V_3Si ,¹³ indicates the presence of low energy quasiparticle excitation due to the quasiclassical Doppler shift.¹⁴ This result strongly suggests that the superconducting order parameter also has an anisotropic (or multi-gapped) structure on the Fermi surface.¹⁵

Nb_3Sn samples were prepared by the method described elsewhere.¹⁶ The superconducting transition temperature was determined to be 17.9(2) K, as inferred from the shielding effect in magnetization measurement. Several single crystals with a sizable dimension ($\sim 10^2$ mg each, covering a beam spot area of $7 \times 7 \text{ mm}^2$ with random crystal orientation) were used for μSR measurement with a high transverse field spectrometer (HiTime) installed on the M15 beamline of TRIUMF, Canada, where they were irradiated by a muon beam of 4 MeV. Further details on the μSR measurements using HiTime might be found in earlier publications.¹⁷ One of these crystals, which was confirmed to be of single domain at ambient temperature, was used for the neutron measurements with the SANS-J spectrometer of JRR-3, Japan Atomic Energy Agency. In both measurements, precautions were taken to minimize the effect of flux pinning: every time when external magnetic field was changed, the sample temperature was raised above T_c and cooled down again after the magnetic field was settled. The magnetic field dependence was obtained for transverse field μSR spectrum (TF- μSR , where the initial muon spin polarization is perpendicular to the external field) at 2.0–2.5 K and for SANS spectrum at 2.6(1) K, respectively.

Since we can reasonably assume that implanted muons (with 4 MeV) stop randomly on the length scale of FLL (which is 20–200 nm over the relevant field range), TF- μSR signal provides a random sampling of the internal field distribution $B(\mathbf{r})$, $\hat{P}(t) = \exp(-\sigma_p^2 t^2) \int_{-\infty}^{\infty} n(B) \exp(i\gamma_{\mu} B t - i\phi) dB$, with $n(B) = \langle \delta(B - B(\mathbf{r})) \rangle_{\mathbf{r}}$, where σ_p is the additional relaxation due to random flux pinning, $n(B)$ is the spectral density for the internal field defined as a spatial average ($\langle \rangle_{\mathbf{r}}$) of the delta function over a unit cell of FLL, γ_{μ} is the muon gyromagnetic ratio ($= 2\pi \times 135.53 \text{ MHz/T}$), and ϕ is the initial phase of rotation.¹⁸ These equations indicate that the real amplitude of the Fourier transformed muon spin precession signal corresponds to the spectral density, $n(B)$. In the modified London model, which is a good approximation to evaluate $B(\mathbf{r})$ at relatively lower

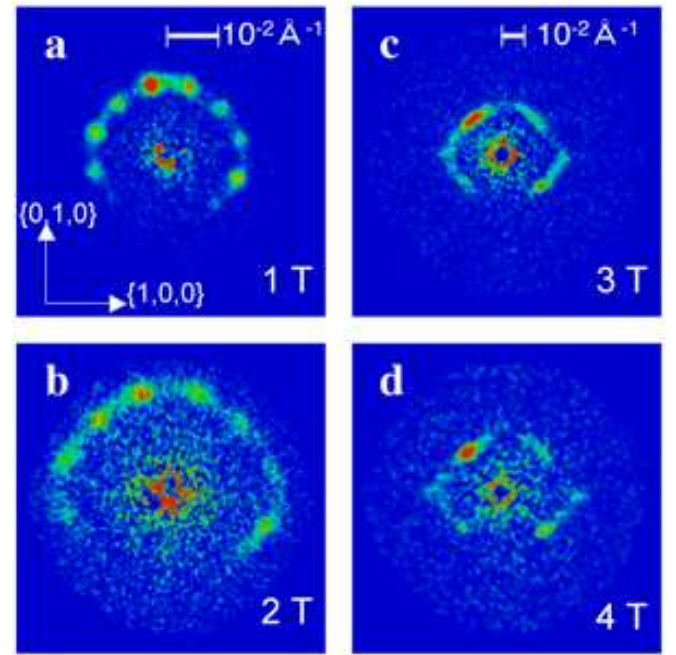


FIG. 2: SANS diffraction patterns obtained by subtracting the background data at 30 K from the data taken at 2.6(1) K after field cooling for an external magnetic field $\mu_0 H = 1 \text{ T}$ (a), 2 T (b), 3 T (c), and 4 T (d) (raw data). The crystal c -axis is aligned to neutron beam, and one of the $\{1,0,0\}$ in-plane axis is aligned to the horizontal axis in the plane perpendicular to the field.

external fields ($\mu_0 H \ll H_{c2}$)¹⁹, $B(\mathbf{r})$ is given by a sum of the magnetic induction from isolated vortices to yield

$$B(\mathbf{r}) = \sum_{\mathbf{K}} b(\mathbf{K}) \exp(-i\mathbf{K} \cdot \mathbf{r}) \quad (1)$$

$$b(\mathbf{K}) = B_0 \frac{\exp(-K^2 \xi_v^2)}{1 + K^2 \lambda^2 + (\overline{n}_{xxyy} K^4 + \overline{d} K_x^2 K_y^2) \lambda^4}, \quad (2)$$

where \mathbf{K} are the vortex reciprocal lattice vectors, B_0 ($\simeq \mu_0 H$) is the average internal field, λ is the *effective* London penetration depth, ξ_v is the cutoff parameter for the magnetic field distribution near the vortex cores, and \overline{n}_{xxyy} and \overline{d} are dimensionless parameters arising from the nonlocal corrections with the term proportional to $K_x^2 K_y^2$ controlling the fourfold anisotropy: the overline denotes an averaging of the parameter over the polar angle of the symmetry axis, as it is anticipated for a mosaic of crystals.¹¹ It is evident in Eq.(1) that $b(\mathbf{K})$ is a spatial Fourier component of $B(\mathbf{r})$. The model predicts an asymmetric field profile for $n(B)$ characterized by a negatively shifted sharp cusp due to the van Hove singularity associated with the saddle points of $B(\mathbf{r})$ and an asymptotic tail towards higher fields where the maximal field is determined by $B(|\mathbf{r} - \mathbf{r}_i| \sim \xi_v)$ (with \mathbf{r}_i being the vortex centers).

Examples of the fast Fourier transform (FFT) of μSR spectra at several external magnetic fields are shown in Fig. 1, where one can readily observe the asymmetric

lineshape with slight smearing due to the random pinning of vortices, random local fields from nuclear moments, and the limited time window for FFT ($\sim 4 \mu\text{s}$: note that such smearing is irrelevant for the analysis in time domain). Based on the least-square method with appropriate consideration of the statistical uncertainty, the μSR spectra are compared in time domain with those calculated by using Eqs.(1)–(2) to deduce a set of parameters, σ_p , λ , ξ_v , \bar{n}_{xxyy} , and \bar{d} : a typical example is shown in Fig. 1. For the reconstruction of $B(\mathbf{r})$ from $n(B)$, one needs to know the two-dimensional structure of FLL obtained from other experimental techniques including SANS. In particular, it is noticeable in Fig. 1 that the peak due to the saddle points exhibits a steep change with increasing external field from 2 T to 3 T, suggesting an anomaly in the FLL structure. As shown below, this speculation is confirmed by SANS measurements over the region of relevant magnetic field.

In a SANS experiment, a FLL gives rise to Bragg reflections at reciprocal lattice points, $\mathbf{K} = l\mathbf{u} + m\mathbf{v} = \mathbf{K}_{lm}$. The intensity of a single reflection (l, m) is given by $|b(\mathbf{K})|^2/|\mathbf{K}_{lm}|$. Considering Eq.(2), it is reduced to $I_{10} \propto d_{10}\Phi_0^2/\lambda^4$ for a first order reflection, where $K_{10} = 2\pi/d_{10}$ with d_{10} being the FLL interval ($= \sqrt{3}a_0/2$ for a hexagonal FLL) and Φ_0 is the flux quantum. Fig. 2 shows the typical SANS-J data at 2.6(1) K after subtracting background data obtained at 30 K ($> T_c$, which is far below T_M), where scattered neutrons from an incident beam with a mean wavelength $\lambda_0 = 6.5 \text{ \AA}$ ($\Delta\lambda_0/\lambda_0 \simeq 0.13$ FWHM, collimated within a diameter of 2 mm) are detected by a position-sensitive detector (consisting of 128×128 pixels with each pixel size being $4.95 \times 5.08 \text{ mm}^2$, covering a sensitive area of 58 cm²) at a distance of 10 m (1–2 T) or 4 m (3–4 T) from the specimen. One of the crystal *c*-axes and external magnetic field are aligned together to the neutron beam. The cryostat (including the magnet) and specimen are rotated slightly ($\pm 0.2^\circ$, in several steps) around the vertical axis to obtain a sum of diffraction patterns over Bragg angles for both triangular and square FLL structure. It is clear in Fig. 2 that there is a difference in the pattern of angles between data at 1–2 T and those at 3–4 T. Since the patterns at lower fields suggests an overlap of two (possibly distorted) hexagonal domains due to the tetragonal crystal structure, their change into the nearly four-fold symmetric pattern at higher fields demonstrate the occurrence of triangular-to-square lattice transformation at 2–3 T. The field range of transformation is considerably higher than that in V₃Si, where the transition to square lattice is nearly complete at 1.5 T (with $H \parallel \{0,0,1\}$).⁹ As shown in Fig. 4d, the apex angle of the real space unit cell is evaluated to be indeed close to 60° and 90° for the respective data. Furthermore, the spots on the $\{1,0,0\}$ axis at high fields (Figs. 2c, d) is absent at lower fields. This clearly indicates that the diagonal of the real space rhombic unit cell, which is aligned to $\{1,1,0\}$ or $\{1,\bar{1},0\}$ direction in each domain, rotates to a $\{1,0,0\}$ direction with increasing field. A similar domain structure at lower

field has been observed in V₃Si.^{9,20}

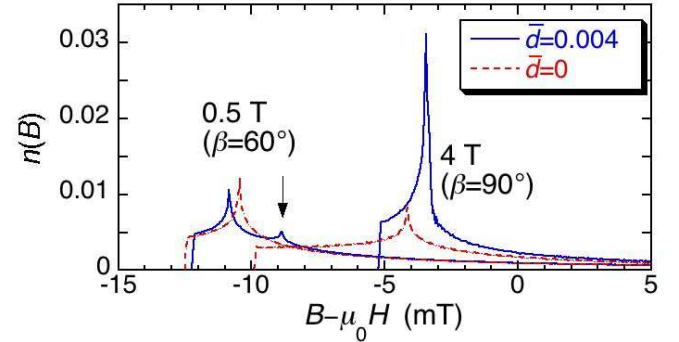


FIG. 3: Spectral density distribution $n(B)$ calculated for a hexagonal FLL with ($\bar{d} = 0.004$) or without ($\bar{d} = 0$) non-local correction under an external field of 0.5 T (where $\lambda = 83.5 \text{ nm}$, $\xi_v = 3.1 \text{ nm}$, and $\bar{n}_{xxyy} = 0$). The sharp peaks are due to van Hove singularities arising from turning points in $B(\mathbf{r})$, where $\vec{\nabla}B(\mathbf{r}) = \mathbf{0}$. An additional peak (labeled by arrow) appears for the former case because of the incommensurability between triangular FLL and squared shape of $B(\mathbf{r})$ around a vortex. Those for a square FLL at 4 T are shown for comparison ($\lambda = 100.0 \text{ nm}$, $\xi_v = 2.8 \text{ nm}$, and $\bar{n}_{xxyy} = 0$).

Once the FLL structure is resolved by SANS measurements, high quality μSR spectra can provide rich information on the mixed state though the detailed mapping of $B(\mathbf{r})$; as it has been demonstrated in the earlier works^{13,21}, the lineshape strongly depends on λ , ξ_v , \bar{n}_{xxyy} and \bar{d} in Eq.(2) and thereby they can be deduced by fitting analysis without much ambiguity. In particular, as shown in Fig. 3, the spectral weight for the lower field side of the van Hove singularity strongly depends on the magnitude of \bar{d} for the square FLL. Besides these, we need to introduce two more parameters to describe the reciprocal vectors which undergo transformation: the apex angle, β , and the mean width for the FLL distortion, σ_K ,²² to describe the fluctuation of the reciprocal vectors, $\mathbf{K} = l(1 + \delta_l)\mathbf{u} + m(1 + \delta_m)\mathbf{v}$ with a probability distribution function, $P(\delta_k) \propto \exp(-\delta_k^2/\sigma_K^2)$ ($k = l, m$). The last parameter effectively serves to add a Lorentzian-type broadening to $n(B)$ and thereby discernible from the Gaussian broadening due to local disorder (which is described by σ_p). The randomness associated with the mosaic crystals is presumed to be represented by σ_K . Fig. 4 shows the field dependence of those parameters, where (a) λ , (b) ξ_v , (e) \bar{n}_{xxyy} and \bar{d} are directly related with the local structure of supercurrent around a single flux line, whereas others are with the morphology of the FLL. It is inferred from the behavior of σ_K (Fig. 4c) that a strong long-range distortion occurs over a field range of 2–4 T, where the FLL structure undergoes transformation between triangular and square lattice. The anomalous enhancement of λ observed in Fig. 4a is probably due to the artifact associated with this distortion; the reduced chi-square exceeds 1.5 around 3 T while it is typically 1.2–1.4 for $\mu_0 H < 2 \text{ T}$ or $\mu_0 H > 4 \text{ T}$ (see Fig. 4f). Similar scat-

tering of the parameter value is also noticeable in ξ_v , σ_p , and \bar{d} over the relevant field range, which may represent the systematic uncertainty due to the distortion. However, except for these anomalies, we can observe a clear trend in all of the parameters. Namely, λ exhibits a gradual increase with increasing magnetic field below ~ 2 T (which we discuss below in more detail), while ξ_v tends to decrease slightly at lower fields and levels off above ~ 2 T. The behavior of ξ_v , which to some extent represents that of the effective vortex core radius, is commonly found in various superconductors, which is attributed to the stronger overlapping of supercurrents around vortex center and intervortex transfer of quasiparticles.²³ The magnitude of ξ_v at lower field is in good agreement with the Ginzburg-Landau coherence length, $\xi_{\text{GL}} \simeq 39$ Å deduced from the relation $H_{c2} = \Phi_0/2\pi\xi_{\text{GL}}^2$ [with $H_{c2}(2$ K) being assumed to be 22 T]. As is anticipated from the SANS result, β exhibits a steep change from 60° to 90° around 2–3 T. The behavior is qualitatively in good agreement with the prediction of the non-local model (solid curve^{11,12}, where the critical field is assumed to be 3 T). Thus, it indicates that the anisotropic flow of the supercurrent due to the nonlocal effect is the primary origin of the square-lattice formation at higher fields. The magnitude of \bar{d} ($\simeq 4 \times 10^{-3}$), which should be regarded as a lower boundary considering the fact that it is reduced by an averaging over a varying symmetry axis,¹¹ is considerably larger than that observed in V₃Si ($\simeq 0.3\text{--}1 \times 10^{-3}$),¹³ suggesting a stronger anisotropy in the Fermi surface. The spin relaxation due to the random local distortion (σ_p) exhibits a gradual decrease with increasing field: this is qualitatively understood as a result of stronger overlap of flux lines at higher field that makes less room for flux lines to deviate away from the regular position. Unfortunately, the SANS data are available only up to 5 T due to experimental conditions, and therefore the origin of the weak anomaly around 5.5 T (see Fig. 4c) is not identified at this stage.

It is interesting to note that the anisotropy parameter \bar{d} is sharply reduced to zero below ~ 2 T: a similar behavior is reported for V₃Si.¹³ As shown in Fig. 4f, a comparative analysis with \bar{d} fixed to 0.004 (\sim an average for $\mu_0 H > 2$ T) yields systematic increase of chi-squares, while little variation is found for other parameters. This is attributed to an additional cusp in $n(B)$ (see Fig. 3) corresponding to the saddle points relatively near the vortex cores where $B(\mathbf{r})$ is influenced by the squared shape of supercurrent flow. Our result indicates that the field profile over the field range of hexagonal FLL may be better described by the isotropic London model.

Now, we discuss the origin of gradual increase of λ in Fig. 4a. Our systematic study on the magnetic field dependence of λ in various superconductors indicates that the gradient ($d\lambda/dH$) provides information on the low energy quasiparticle excitations.¹⁵ In the mixed state, the quasiparticle momentum \mathbf{v}_F is shifted by the flow of supercurrent \mathbf{v}_s around the vortices due to a semi-classical Doppler shift, leading to a shift of the quasiparticle en-

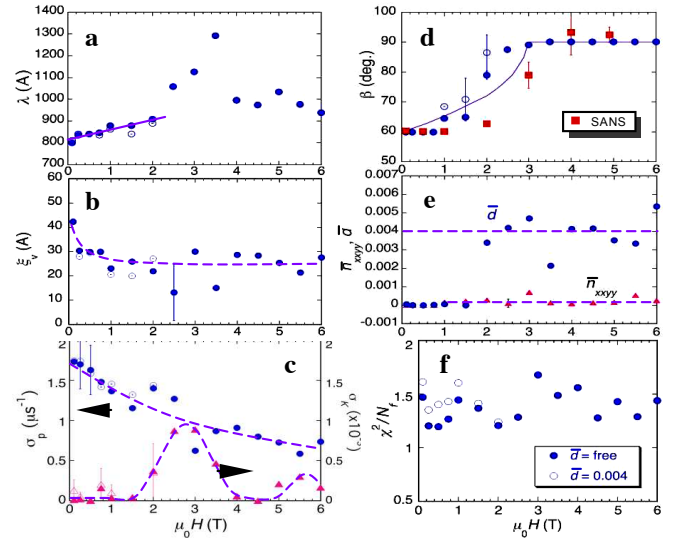


FIG. 4: Magnetic field dependence of various parameters to describe the field distribution $B(\mathbf{r})$ obtained by analyzing TF- μ SR spectra using the modified London model: (a) the effective London penetration depth (λ), (b) the cutoff parameter (ξ_v), (c) the enhanced relaxation rate due to local disorder of FLL (σ_p), and the mean width for the long-range distortion (σ_K), (d) the apex angle of the rhombic unit cell in the real space (together with the SANS data), and (e) the dimensionless parameters to describe anisotropy of supercurrent density around the flux lines (\bar{n}_{xxyy} , \bar{d}). Error-bars in (a)–(e) show statistical errors (those not shown are smaller than the symbol size), whereas the scatter of points, particularly for 2–4 T, may represent systematic uncertainty (see text). The reduced chi-squares are shown in (f). The open symbols in (a)–(d) and (f) (only for $\mu_0 H \leq 2$ T) are those obtained by fixing \bar{d} to 0.004. Dashed lines are merely intended to guide for eyes. [See text for the solid lines in (a) and (d).]

ergy spectrum to an amount $\varepsilon = m\mathbf{v}_F \cdot \mathbf{v}_s$. When the superconducting order parameter has a nodal structure or anisotropy (including multi-gap), the Cooper pairs with a gap energy of less than ε can be broken by the Doppler shift,^{14,24} leading to an enhancement of λ . Using a normalized magnetic field, $h = H/H_{c2}$, we can express the field dependence of λ ,

$$\lambda(h) = \lambda(0)[1 + \eta \cdot h], \quad (3)$$

where η is the dimensionless parameter to represent the gradient (the magnitude of pair breaking effect). Since $\lambda^{-2}(h) = 4\pi e^2 n_s(h)/m^* c^2$ that is determined by the superfluid density, $n_s(h)$, the reduction of $n_s(h)$ due to the Doppler shift would lead to the increase of $\lambda(h)$. A fitting analysis of the data in Fig. 4a by Eq.(3) below 2 T yields $\eta = 1.24(2)$ with $\lambda(0) = 818(1)$ Å, where the result is shown by a solid line in Fig. 4a. Considering that no clear evidence is reported for the presence of nodes in the order parameter, the situation in Nb₃Sn is close to the case of MgB₂ where a similar trend of $\lambda(h)$ with $\eta \simeq 1.3$ was observed.¹⁷ Since μ SR measurements are made at finite temperature (T), the Cooper pairs hav-

ing the energy near the gap minimum (or a smaller gap) Δ_s would be susceptible to excitation due to the Doppler shift when $\Delta_s \leq k_B T$.²⁴ Interestingly, an earlier report on electronic Raman scattering experiment suggests a relatively strong gap anisotropy ($\sim 20\%$) in Nb_3Sn , whereas no such anomaly seems to exist for V_3Si .²⁵ Meanwhile, a very recent specific heat measurement in Nb_3Sn demonstrated the presence of residual excitation below $\sim 0.3T_c$, which they attributed to a double-gapped order parameter with $\Delta_s = 0.61(5)$ meV.²⁶ Our result is another, yet microscopic evidence for the anisotropic (or multi-gapped) s -wave pairing for the order parameter of Nb_3Sn . The anisotropy of the Fermi surface revealed by FLL transformation may be related with the structure of the order parameter. Further study using the techniques sen-

sitive to gap anisotropy would be helpful to determine the gap structure in full detail.

In summary, we have obtained detailed mapping of the local magnetic field in the mixed state of Nb_3Sn using μSR and SANS, from which we extracted fundamental length scales of superconductivity. Unlike V_3Si , the field-induced enhancement of the effective penetration depth strongly suggests that the order parameter in Nb_3Sn has a structure, either anisotropic or multi-gapped.

We would like to thank the staff of TRIUMF for their technical support during the μSR experiment. This work was partially supported by a Grant-in-Aid for Scientific Research on Priority Areas and a Grant-in-Aid for Creative Scientific Research from the Ministry of Education, Culture, Sports, Science and Technology of Japan.

¹ B. T. Matthias *et al.*, Phys. Rev. **95**, 1435 (1954).
² B. T. Matthias *et al.*, Phys. Rev. **139**, A1501 (1965).
³ L. R. Testardi, Rev. Mod. Phys. **47**, 637 (1975).
⁴ M. Weger and I. B. Goldberg, in *Solid State Physics: Advances in Research and Applications*, Vol. 28, 2 (Academic, New York, 1973).
⁵ P. B. Allen, in *Dynamical Properties of Solids*, Vol. 3, 95 (North-Holland, Amsterdam, 1980).
⁶ R. Mailfert *et al.*, Phys. Lett. **24A**, 315 (1967).
⁷ G. Shirane *et al.*, Solid State Commun. **9**, 397 (1971).
⁸ J. D. Axe and G. Shirane, Phys. Rev. B **8**, 1965–1977 (1973).
⁹ M. Yethiraj *et al.*, Phys. Rev. Lett. **82**, 5112 (1999).
¹⁰ C. E. Sosolik *et al.*, Phys. Rev. B **68**, 140503(R) (2003).
¹¹ V. G. Kogan *et al.*, Phys. Rev. Lett. **79**, 741 (1997).
¹² V. G. Kogan *et al.*, Phys. Rev. B **55**, R8693 (1997).
¹³ J. E. Sonier *et al.*, Phys. Rev. Lett. **93**, 017002 (2004).
¹⁴ G. E. Volovik, Pis'ma Zh. Eksp. Teor. Fiz. **58**, 457 (1993) [JETP Lett. **58**, 469 (1993)].
¹⁵ R. Kadono, J. Phys.: Condens. Matt. **16**, S4421 (2004).
¹⁶ Y. Fujii *et al.*, Phys. Rev. B **25**, 364 (1982).
¹⁷ K. Ohishi *et al.*, J. Phys. Soc. Jpn. **72**, 29 (2003).
¹⁸ E. H. Brandt, Phys. Rev. B **37**, R2349 (1988).
¹⁹ V. Fesenko *et al.*, Physica C **211**, 343 (1993).
²⁰ D. K. Christen *et al.*, Physica **135B**, 369 (1985).
²¹ K. Ohishi *et al.*, Phys. Rev. B **65**, 140505 (2002).
²² R. Kadono *et al.*, Phys. Rev. B **63**, 224520 (2001).
²³ J. E. Sonier, J. Phys.: Condens. Matter **16**, S4499 (2004).
²⁴ N. Nakai *et al.*, Phys. Rev. B **70**, 100503(R) (2004).
²⁵ S. B. Dierker *et al.*, Phys. Rev. Lett. **50**, 853 (1983).
²⁶ V. Guritanu *et al.*, Phys. Rev. B **70**, 184526 (2004).